Ion Dynamics in Ionic-Liquid-Based Li-Ion Electrolytes Investigated by Neutron Scattering and Dielectric Spectroscopy

Charl J. Jafta,[a] Craig Bridges,[a] Leon Haupt,[b] Changwoo Do,[c] Pit Sippel,[b] Malcolm J. Cochran,[c] Stephan Krohns,[b] Michael Ohl,[d] Alois Loidl,[b] Eugene Mamontov,*[c] Peter Lunkenheimer,*[b] Sheng Dai,*[a, e] and Xiao-Guang Sun*[a]

A detailed understanding of the diffusion mechanisms of ions in pure and doped ionic liquids remains an important aspect in the design of new ionic-liquid electrolytes for energy storage. To gain more insight into the widely used imidazolium-based ionic liquids, the relationship between viscosity, ionic conductivity, diffusion coefficients, and reorientational dynamics in the ionic liquid 3-methyl-1-methylimidazolium bis(trifluoromethanesulfonyl)imide (DMIM-TFSI) with and without lithium bis(trifluoromethanesulfonyl)imide (Li-TFSI) was examined. The diffusion coefficients for the $DMIM^+$ cation and the role of ion aggregates were investigated by using the quasielastic neutron scattering (QENS) and neutron spin echo techniques. Two diffusion mechanisms are observed for the $DMIM^+$ cation with and without Li-TFSI, that is, translational and local. The data additionally suggest that Li^+ ion transport along with ion aggregates, known as the vehicle mechanism, may play a significant role in the ion diffusion process. These dielectric-spectroscopy investigations in a broad temperature and frequency range reveal a typical α–β-relaxation scenario. The α relaxation mirrors the glassy freezing of the dipolar ions, and the β relaxation exhibits the signatures of a Johari–Goldstein relaxation. In contrast to the translational mode detected by neutron scattering, arising from the decoupled faster motion of the $DMIM^+$ ions, the α relaxation is well coupled to the dc charge transport, that is, the average translational motion of all three ion species in the material. The local diffusion process detected by QENS is only weakly dependent on temperature and viscosity and can be ascribed to the typical fast dynamics of glass-forming liquids.

Introduction

Ionic liquids (ILs) are a unique class of materials having organic cations paired with weakly coordinating inorganic or organic anions and are defined as having a melting point below 100 °C. These materials exhibit a characteristic set of properties, including low vapor pressure, low flammability, wide electrochemical stability windows, and high ionic conductivities, which makes them suitable as solvents for organic and inorganic synthesis as well as various large-scale industrial chemical processes, and as electrolytes for electrical energy storage applications.[1] Although the intrinsic high ionic conductivity of ILs is beneficial for energy storage applications, their cations and anions usually do not participate in the electrochemical reactions. As a result, they can potentially interfere with electroactive species such as Li^+, Na^+, and Al^{3+} during the electrochemical reaction process at the electrode/electrolyte interface, as the organic cation of the ionic liquids travels in the same direction as the electroactive cation, and thus high polarization results.[1g,2] This is especially true when a low concentration of salt is dissolved in the IL. For example, it has been shown by using the pulsed-field-gradient NMR technique that the lithium

[a] C. J. Jafta, C. Bridges, S. Dai, X.-G. Sun
Chemical Science Division
Oak Ridge National Laboratory
Oak Ridge, TN 37831 (USA)
E-mail: dais@ornl.gov
sunx@ornl.gov

[b] L. Haupt, P. Sippel, S. Krohns, A. Loidl, P. Lunkenheimer
Experimental Physics V, Center for Electronic Correlations and Magnetism
University of Augsburg
86159 Augsburg (Germany)
E-mail: peter.lunkenheimer@physik.uni-augsburg.de

[c] C. Do, M. J. Cochran, E. Mamontov
Neutron Scattering Division, Oak Ridge National Laboratory
Oak Ridge, TN 37831 (USA)
E-mail: mamontove@ornl.gov

[d] M. Ohl
Jülich Centre for Neutron Science
Forschungszentrum Jülich
52428 Jülich (Germany)

[e] S. Dai
Department of Chemistry, University of Tennessee
Knoxville, TN 37996 (USA)

Supporting Information and the ORCID identification number(s) for the author(s) of this article can be found under: https://doi.org/10.1002/cssc.201801321.

transference number is usually less than 0.1 when the molar fraction of lithium is less than 0.2.[3] We infer that one of the effective ways to enhance lithium transference number in IL electrolytes is to increase the molar fraction of lithium, simply by increasing the salt concentration. However, the consequence is a higher viscosity and lower ionic conductivity.[4] Given these performance tradeoffs as a function of concentration, it is crucial to understand how the ions move effectively within these ionic media. This may open a route to optimizing the structure of ILs and the salt concentration to improve the cycling performance of batteries containing IL electrolytes.

So far, different techniques, such as molecular dynamics modeling,[4b,5] Raman spectroscopy,[6] pulsed-field-gradient NMR spectroscopy,[1h,7] electrophoretic NMR spectroscopy,[8] and heteronuclear Overhauser NMR spectroscopy,[9] have been used to investigate the fundamental lithium transport mechanism in IL electrolytes. One common finding is severe ion aggregation in salt-doped IL electrolytes. In particular, Li et al. found in *N*-methyl-*N*-propylpyrrolidinium bis(trifluoromethanesulfonyl) imide doped with lithium bis(trifluoromethanesulfonyl)imide (Li-TFSI) that at low salt concentration ($x \leq 0.2$) the Li^+ cation was coordinated on average by three or more $TFSI^-$ anions, two of which contribute a single oxygen atom (monodendate) and one contributes two oxygen atoms (bidendate).[5a] At higher salt concentration ($x \geq 0.33$) each Li^+ cation was coordinated by 3.5 anions with fewer bidendate and more monodendate anions in the Li^+ coordination sphere.[5a] In the presence of this ion aggregation, Li^+ ion transport is reported to occur by a combination of two mechanisms: 70% through exchange of $TFSI^-$ anions between the first coordination shell and outer coordination shells of Li^+ (structure-diffusion mechanism) and 30% through Li^+ diffusion with its coordination shell (vehicle mechanism).[5b]

In the present study, we used dielectric spectroscopy and neutron scattering techniques to help understand the ionic dynamics in ILs with and without lithium-salt doping, aiming to elucidate the role played by different diffusion mechanisms in the total ionic conductivity. Specifically, we synthesized the simplest imidazolium-based IL, namely, 3-methyl-1-methylimidazolium bis(trifluoromethanesulfonyl) imide (DMIM-TFSI), and prepared different Li-TFSI salt concentrations in DMIM-TFSI to investigate how lithium salt affects the ion transport in the electrolyte system. We observed various dynamic processes: 1) a fast local process for $DMIM^+$, 2) an aggregate diffusion process involving multiple ions, 3) a dipolar relaxation process, well coupled to the overall translational ion motion, and 4) a Johari–Goldstein relaxation, as commonly found in supercooled liquids. We discuss how these processes are influenced by the salt concentration, temperature and viscosity, and show how the neutron spin echo (NSE), quasielastic neutron scattering (QENS), and dielectric spectroscopy data are both complimentary and distinct.

Experimental Section

DMIM-TFSI was synthesized and purified as reported in Ref. [10]. Li-TFSI was purchased from Aldrich and dried at 150 °C under high vacuum for 12 h before use. Different amounts of Li-TFSI were added to DMIM-TFSI in a glovebox to make the desired salt concentrations (molality $b = 0$, 0.3, 0.5, 0.7, and 1.0 mol kg^{-1}). The samples are hereafter identified by their concentration (0 M, 0.3 M, etc.). The viscosity was measured with a Brookfield DV-II + Pro viscometer. The temperature was controlled by using a water circulating bath, and a minimum of 30 min was allowed for equilibration before each measurement.

Differential scanning calorimetry (DSC) was carried out with a TA Instruments DSC Q100 under nitrogen atmosphere. For each measurement the samples were tightly sealed in aluminum pans and were first equilibrated at 193 K, followed by ramping to 373 K at a heating rate of 10 K min^{-1}. The above process was then repeated, and the glass transition temperatures (T_g, onset point) and melting temperatures (T_m, peak position) were determined.

For dielectric spectroscopy, the sample material was put into parallel-plate capacitors made of stainless steel (typical diameters 5–12 mm) by using glass-fiber spacers to keep the plates at a defined distance of 0.1 mm. To minimize water content, before the dielectric measurements the prepared samples were heated at 100 °C in dry nitrogen atmosphere for up to 20 h, which is an efficient way to remove residual water.[11] During this time, the dielectric response was continuously monitored until constant values were reached, and the actual measurement run was started afterwards. For the dielectric measurements at frequencies $10^0 < \nu < 10^7$ Hz, a frequency-response analyzer (Novocontrol Alpha analyzer) was used. Cooling and heating of the samples was achieved by an N_2-gas cryostat. Additional high-frequency measurements at $10^6 < \nu < 3 \times 10^9$ Hz were performed at room temperature by an *I–V* technique in which the sample capacitor is mounted at the end of a coaxial line bridging inner and outer conductors.[12] For these measurements, an impedance analyzer (Agilent E4991A) was used.

The NSE experiments were carried out in the q range $0.05 \leq q \leq 0.3$ Å^{-1} with a neutron wavelength band of $6 \leq \lambda \leq 9$ Å, for 0, 0.5 M, and 1.0 M ILs.[13] Aluminum sample cells were held inside a vacuum cryostat, and the temperature was controlled by a heating rod to 400, 425, and 450 K. By using polarized neutrons, the coherent scattering $S(q, t)/S(q, 0)$ was directly measured up to Fourier times from 10 ps to 30 ns. QENS measurements were performed at the backscattering spectrometer BASIS of the Spallation Neutron Scattering facility (Oak Ridge National Laboratory) by using a standard setup with an energy resolution of 3.5 μeV (full width at half-maximum) and accessible range of energy transfers of ±100 μeV.[14] IL samples with 0.0 and 1.0 M Li-TFSI were measured on BASIS at various temperatures. Non-deuterated samples were used for both neutron scattering experiments.

Results and Discussion

DSC and viscosity

The thermal properties of the DMIM-TFSI-based electrolytes were evaluated by DSC (Figure 1). For pure DMIM-TFSI, the

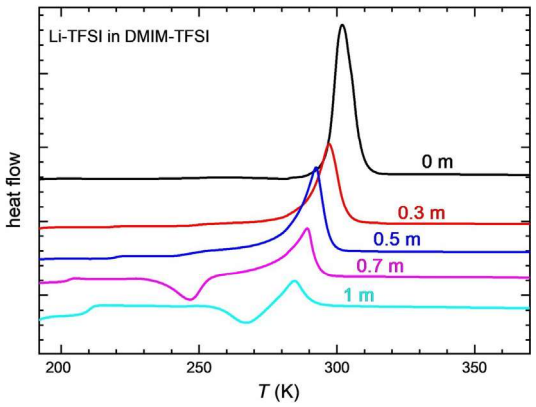

Figure 1. DSC heat flow for various Li-TFSI concentrations. Peaks reveal endothermic and minima exothermic transitions. Curves are shifted vertically for better readability.

DSC curve shows only a single endothermic peak with no indication of a glass-transition anomaly. Clearly, during the cooling process, DMIM-TFSI reaches a fully crystalline state, melting of which leads to the endothermic peak at 302 K. A corresponding melting peak was also found for the samples with admixed Li salt. The melting point decreases to 297, 293, 289, and 284 K when the salt concentration increases to 0.3, 0.5, 0.7, and 1.0 M, respectively. Only for DMIM-TFSI with the highest two salt contents were significant glass-transition anomalies detected, at 203 K for the 0.7 M IL and at 208 K for the 1.0 M IL. Consistent with this finding, the heat flow for these two concentrations exhibits an exothermic minimum due to crystallization, that is, the samples indeed were (at least partly) in the glassy state after cooling. Overall, these results reveal that, in contrast to many other ILs,[15] DMIM-TFSI cannot be easily supercooled and that its glass-forming abilities are enhanced by admixture of Li salt. To avoid problems with crystallization, consequently the neutron-scattering and viscosity measurements were restricted to temperatures close to and above room temperature.

Figure 2 shows the temperature dependence of the viscosity η for the 0 and 1 M ILs from 293 to 353 K. At 303 K, η of DMIM-TFSI without Li salt is about 32 mPa s, and the 1 M IL has a higher viscosity of 63 mPa s. These values are comparable to or even smaller than those for ILs typically used in lithium-ion batteries.[2a,16] The increase of viscosity with increasing Li-salt concentration can be well explained by the high ionic potential (ratio of charge to ion radius) of the Li^+ ion, which should lead to increased interactions between the different ion species.

For glass-forming liquids the temperature dependence of η is often described by the Vogel–Fulcher–Tammann (VFT) equation [Eq. (1)][17]

$$\eta = \eta_0 e^{DT_0/(T-T_0)} \qquad (1)$$

where η_0 is the viscosity at infinite temperature and T_0, where $\eta(T)$ would diverge, is sometimes referred to as an "ideal"

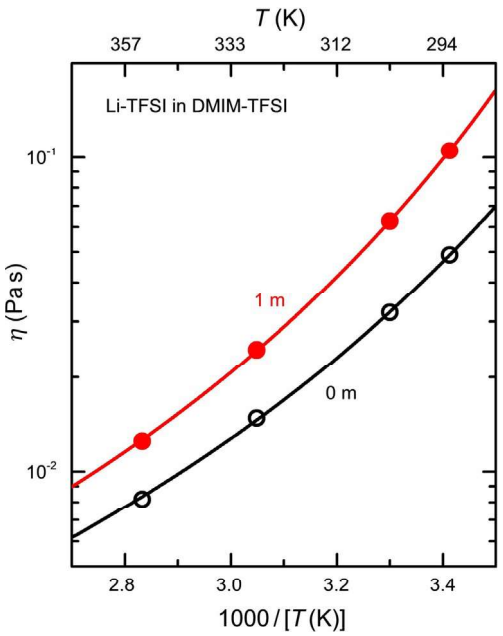

Figure 2. Viscosity of 0 M (empty circles) and 1 M (filled circles) Li-TFSI/DMIM-TFSI as a function of the temperature (Arrhenius plot). The lines are fits with the VFT function [Eq. (1)].

glass-transition temperature, lower than T_g.[18] The lines in Figure 2 reveal that Equation (1) provides good fits of the experimental data (see Table S1 in the Supporting Information for the parameters). The strength parameter D can be used to quantify the characteristic deviation of the system from simple thermally activated behavior, $\eta \propto \exp[E/(k_B T)]$, where E is an energy barrier. Generally, glass formers with high D, the relaxation–time curves of which do not or only weakly deviate from linear behavior in an Arrhenius plot ($\log \eta$ vs. $1/T$), are termed "strong", and those that exhibit a strong curvature are termed "fragile".[17d]

Dielectric spectroscopy

As revealed by Figure S1, in the temperature dependence of the dielectric properties of these ILs, kinks or even jumps occur. These measurements were performed with cooling at 0.6 K min^{-1}, and we ascribe this behavior to full or partial crystallization of the samples. Figure S1 shows that these anomalies are smaller for the higher salt concentrations, and this is consistent with the higher tendency to supercooling for high salt contents found in the DSC experiments (see above). Especially for the 1 M sample, the kinks are nearly negligible for most frequencies and only a small part of the sample seems to crystallize, leaving most of it in the supercooled or glassy state. Thus, the detailed analysis of the frequency-dependent dielectric properties is restricted to this sample.

Figure 3 shows the frequency dependence of the dielectric constant ε', dielectric loss ε'', and the real part of the conductivity σ' of the 1 M sample. In Figure 3 a, a strong increase of $\varepsilon'(\nu)$ with decreasing frequency is observed for temperatures $T \geq 216$ K. For low frequencies at these temperatures, the loss

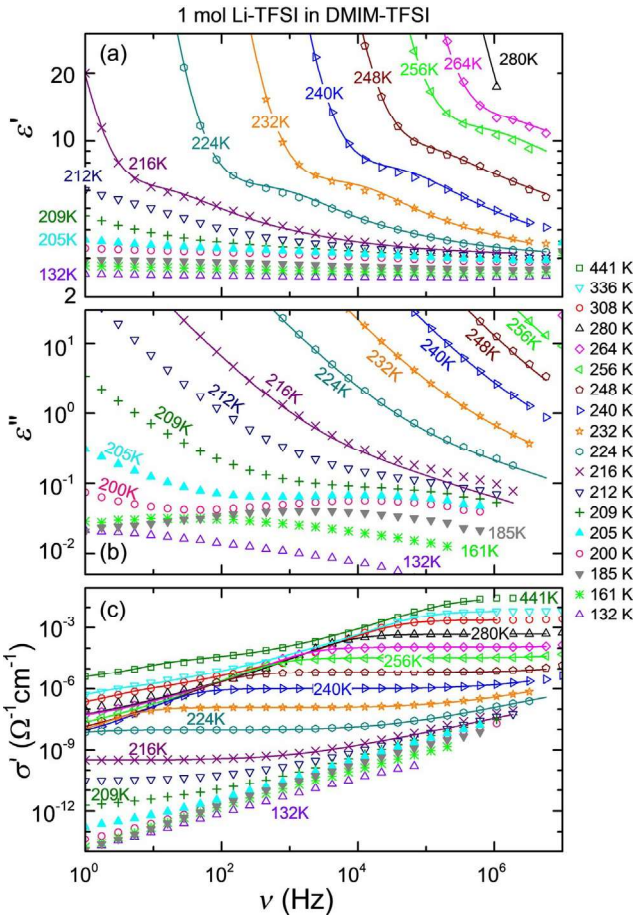

Figure 3. Frequency dependence of the dielectric constant (a), loss (b), and conductivity (c) of DMIM-TFSI with 1 M Li-TFSI. Various spectra are shown for selected temperatures. The lines are fits of the data at $T \geq 216$ K with contributions of the dc conductivity, the α relaxation (modeled by a CD function), and up to two distributed RC circuits accounting for the blocking electrodes.[19] Frames a) and b) show zoomed views of the data concentrating on the intrinsic contributions. For a view of the full spectra, see Figure S2.

finally reaches values as high as 10^5–10^7 (see Figure S2 showing a zoomed-out view of Figure 3). These extremely high values are clearly of non-intrinsic origin and can be ascribed to electrode effects (also termed electrode blocking) arising from the formation of a nearly insulating layer of immobile ions close to the sample/electrode interface.[19] This is a well-known effect for ionic conductors and is not treated in further detail here. Superimposed on this contribution, the $\varepsilon'(\nu)$ curves for $264 \geq T \geq 216$ K in Figure 3a show a steplike feature, which strongly shifts to lower frequencies with decreasing temperature (for lower temperatures, it is shifted out of the investigated frequency window). This is the characteristic behavior of a relaxational process involving the motion of dipolar degrees of freedom, as commonly found, for example, in dipolar supercooled liquids.[12b,20] However, unlike the commonly observed dipolar relaxation in which the amplitude increases with cooling due to the Curie law, the amplitude of the relaxation process in Figure 3a decreases with cooling. This is not the usual behavior of a dipolar relaxation but is often observed for the conductivity relaxation due to local ion rearrangements. Such relaxation features were also previously reported in other ILs.[21] Following previous works,[21a,b,f] we ascribe the observed relaxation mode to the reorientational motions of the dipolar ions. In analogy to the main reorientational dynamics in canonical dipolar liquids,[11] we term it α relaxation in the following. The existence of such reorientational modes in ILs has been clearly proven, for example, by light-scattering spectroscopy.[21d,22] Clearly, just as for conventional dipolar liquids,[12b,20] these modes must lead to corresponding relaxation features in the dielectric spectra (e.g., the observed step in Figure 3a), which may be difficult to discern due to the superposition by contributions from ionic conductivity (because of the general relation $\varepsilon'' \propto \sigma'/\nu$) and electrode polarization.

For relaxational processes, at the point of inflection of the relaxation step in ε', a peak should show up in the loss spectra.[12b,20] However, in Figure 3b this peak cannot be discerned because it is superimposed by the strong dc conductivity of this ionic conductor (the broad peaks observed at the lowest temperatures occur at clearly different frequencies than the steps in ε' and evidence a β relaxation; see below). Owing to the relation $\varepsilon'' \propto \sigma'/\nu$, it leads to a dominant $1/\nu$ divergence of the loss spectra at low frequencies. In Figure 3c, this dc conductivity is directly revealed by the appearance of a clear plateau in $\sigma'(\nu)$ (e.g., between about 10^2 and 10^5 Hz for the 240 K curve). The decrease of $\sigma'(\nu)$ observed at lower frequencies, which is due to the aforementioned electrode blocking, is again a well-known effect for ionic conductors.

Finally, at the lowest investigated temperatures, Figure 3b reveals broad peaks in $\varepsilon''(\nu)$ shifting through the frequency window with temperature. They can be ascribed to a secondary relaxation process, which is a commonly observed phenomenon in conventional dipolar glass-forming liquids[23] and was also previously observed in some ILs.[21a,b,e] Figure 4a shows a zoomed view of the loss in the region of the β relaxation with incusion of spectra at more temperatures than in Figure 3b. As shown by Johari and Goldstein,[24] such faster processes, often termed β relaxations, seem to be a universal feature of glass-forming matter. Various alternative microscopic explanations for the occurrence of these so-called Johari–Goldstein (JG) β relaxations have been proposed, for example, in terms of islands of mobility[24] or small-angle reorientations.[25] Examples of the latter are librational motions of the imidazolium ring, which are suggested to cause β relaxations in a number of 1-hexyl-3-methylimidazolium based ILs.[21c]

As the electrode effects are strongly superimposed on the intrinsic response at $T \geq 216$ K, the spectra at these temperatures in Figure 3 had to be fitted by a corresponding equivalent-circuit model to extract meaningful information on the parameters of the α relaxation. For this purpose, we modeled the blocking electrodes by up to two distributed RC circuits, connected in series to the bulk sample, as described in detail in Ref. [19]. For fitting the intrinsic sample response, we assumed a Cole–Davidson (CD) function,[26] known to provide a good description of the α relaxation in many glass-forming materials[12b,20a,23b] and a dc-conductivity contribution, leading to $1/\nu$ behavior in ε''. The fits were performed simultaneously for ε' and ε''. As revealed by the lines in Figures 3 and 4a and b, this

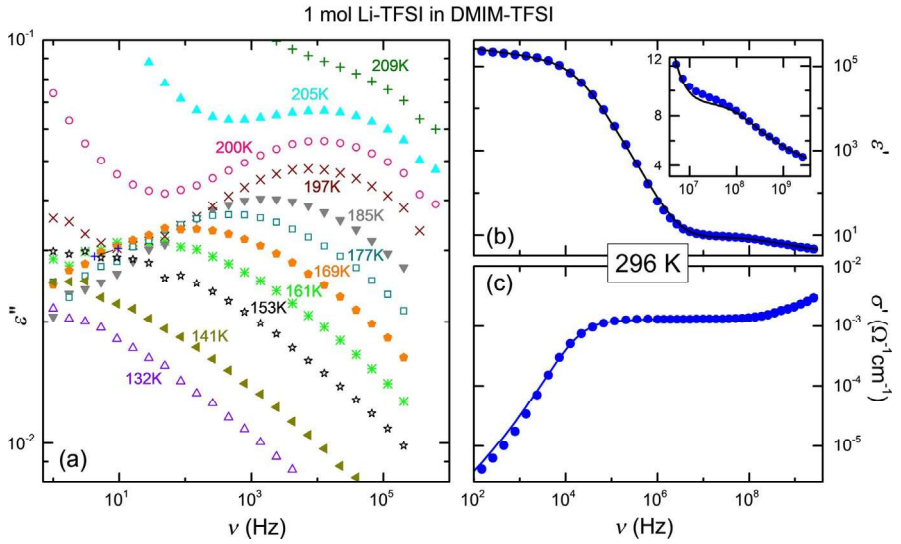

Figure 4. a) Frequency dependence of the dielectric loss of DMIM-TFSI with 1 M Li-TFSI. A zoomed view of the region of the β relaxation is shown for more temperatures than in Figure 3. Broadband spectra of the dielectric constant (b) and loss (c) at room temperature. The lines are fits with the same model as the fits shown in Figure 3. The inset shows a zoomed view of the high-frequency region, in which the α-relaxation step is revealed.

approach clearly provides a reasonable description of the experimental data in the whole frequency range. The deviations seen at the highest frequencies in ε'' at 216 K are due to the onset of the β relaxation, which was not included in the fits.

To reveal information on the α relaxation at room temperature and enable a better comparison with the neutron-scattering results presented below, we performed additional high-frequency measurements extending up to 3 GHz (Figure 4b and c). These spectra were fitted in the same way as those shown in Figure 3 (lines in Figures 4b and c), and this again led to a reasonable description of the experimental data. As shown by the inset of Figure 4b, the α relaxation, which is detected in the range of 100 MHz to 1 GHz, reflects the high dipolar mobility at room temperature. Dielectric data of ionic conductors are sometimes analyzed in terms of the modulus formalism,[27] by considering the complex dielectric modulus $M^* = 1/(\varepsilon' - i\varepsilon'')$ (see Refs. [21d, e, 28] for some examples in ILs). In the present ILs at least three superimposed dynamic processes contribute to the dielectric spectra, namely, reorientational α and β relaxation and translational ion motion. Ionic charge transport is known to lead to separate peaks in M'' spectra, like reorientational relaxation processes, which makes proper assignment and deconvolution difficult. Moreover, the interpretation of the charge-transport-related peak in M'' is rather controversial,[29] and thus we refrain from providing such an analysis here. Both data representations, modulus and permittivity, of course contain the same information.

DC conductivity

From the fits of the dielectric spectra (lines in Figure 3) and by simply reading off the plateau values in $\sigma'(\nu)$ (Figure 3c), the dc conductivity σ_{dc} can be determined. The results for four salt concentrations are provided in Figure 5. The shown data are restricted to sufficiently high temperatures at which (partial)

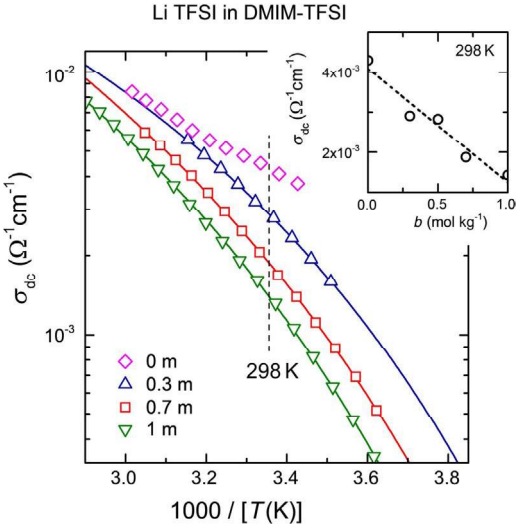

Figure 5. The dc conductivity as a function of temperature of DMIM-TFSI without and with different concentrations of Li-TFSI. The lines are fits with the VFT equation. The inset shows the dependence of the dc conductivity on the salt concentration; the dashed line is a linear fit.

crystallization of the samples, which occurs especially for low salt concentrations (cf. Figure S1), can be excluded. Generally, the ionic conductivity of any electrolyte can be described by Equation (2):[30]

$$\sigma = \sum_i n_i q_i \mu_i \qquad (2)$$

where n_i, q_i, and μ_i are the number, charge, and mobility of the individual charge carrier, respectively. For DMIM-TFSI, the charge carriers are the $DMIM^+$ cations and $TFSI^-$ anions, whereas for the salt-containing IL solutions the additional Li^+ cations also contribute to the charge transport. For the sam-

ples with Li-TFSI, the temperature-dependent ionic conductivity can be well described by a modified VFT equation [Eq. (1)] in which the viscosities η and η_0 are replaced by conductivities σ and σ_0, respectively (solid lines in Figure 5).[31] The 0 M IL may be better described by an Arrhenius law, but the covered temperature range is too small to make a clear statement. VFT behavior of $\sigma_{dc}(T)$ is often found for ILs, reflecting the glasslike freezing of ionic dynamics.[21a,d,32] Figure 5 shows a significant decrease of the dc conductivity with increasing salt concentration. As an example, the concentration-dependent variation of σ_{dc} at room temperature is shown in the inset. It decreases roughly linearly from about 4.1×10^{-3} to $1.3\times10^{-3}\ \Omega^{-1}\,cm^{-1}$. These ionic conductivities are close to that of a conventional carbonate electrolyte used in lithium-ion batteries, that is, $4.8\times10^{-3}\ \Omega^{-1}\,cm^{-1}$ for 1.0 M $LiPF_6$ dissolved in ethylene carbonate/dimethyl carbonate/diethyl carbonate (1:1:1 *v/v/v*).[33] Like the increase of viscosity (Figure 2), the observed decrease of ionic conductivity with increasing salt concentration can be attributed to the stronger interactions between ions, caused by the introduction of the small Li^+ cation with high ionic potential, which implies a lower carrier mobility. This is consistent with the strong decrease of ionic conductivity with decreasing anion radius reported for a number of 1-hexyl-3-methylimidazolium-based ILs with the same cation and different anions.[21c] Although this mechanism corresponds to a reduction of the ionic mobility μ [cf. Eq. (2)], increased formation of ion aggregates triggered by Li addition cannot be excluded,[5b] which would correspond to a reduction of the number of free charge carriers *n*. Overall, large ion aggregates are likely to exist in electrolytes with high salt concentration, but the detailed transport mechanism is still a matter of debate.

Neutron scattering

To directly detect the ion motion and relate it to the Li^+ ion transport mechanism,[34] we used QENS and NSE measurements. The signal in QENS experiments is sensitive to the incoherent neutron scattering cross section of an element. As hydrogen has an exceptionally high incoherent scattering cross section, QENS is very sensitive to hydrogen motion. Whereas the IL DMIM-TFSI has nine hydrogen atoms in the cation, no hydrogen is present in the $TFSI^-$ anion. Thus, the diffusion coefficients calculated from the QENS data can be interpreted as self-diffusion coefficients of the $DMIM^+$ cations.

The QENS data of the 0 and 1 M ILs at 303, 328, and 353 K are shown in Figure S3. The same data sets converted to imaginary part of the dynamic susceptibility, $I(q,E)=S(q,E)/[n_B(E)+1]\approx(E/k_BT)S(q,E)$, are shown in Figure S4. The susceptibility spectra exhibit a peak at about 1 μeV with a fairly strong *q* dependence of the peak position, characteristic of translational diffusivity, the slowest measurable process. At about 10 μeV, a shoulder with strongly *q* dependent intensity, characteristic of a localized mobility, indicates a faster dynamic process. Finally, near the cutoff of the accessible energy-transfer range of about 100 μeV, there is evidence of the tail of yet another dynamic process, too fast to be resolved in the current experiment, also with a fairly strong *q* dependence of intensity, characteristic of a localized mobility. The susceptibility spectra suggest that two dynamic components may be resolvable within the dynamic range of the experiment, on the 1 μeV and 10 μeV scale, and another, much faster component, that cannot be determined reliably, but likely necessitate the use of a background term in the fits.

In a typical QENS experiment, the limited dynamic range significantly restricts the maximum number of fit parameters, oftentimes imposing a choice between a single stretched or two Debye-like components, as it is usually impossible to use more than one stretched fit component. The choice can be made by direct comparison of fit quality, or on the grounds of the appearance of the dynamic susceptibility spectra, which sometimes can distinguish between single- or double-component scenarios, as is the case with the present data sets.

The formalism used for analysis of QENS data from liquids by means of two Debye-like components has been discussed in detail.[35] In brief, assuming that the faster and slower motions of hydrogen-bearing cations can be treated as independent, for each *q* one can write the intermediate scattering function as a simple product, $F(t)=T_1(t)T_2(t)$, and the scattering function as a convolution, $S(E)=T_1(E)*T_2(E)$, where T_1 and T_2 represent different motions. One can approximate the functional form for the faster spatially constrained process by Equation (3):

$$T_1(t) = p + (1-p)\exp\left[-\frac{t}{\tau_1}\right] \tag{3}$$

where τ_1 is a *q*-dependent relaxation time. The parameter *p* describes the *q*-dependent fraction of "elastic" scattering for the transiently constrained translational diffusion process, commonly known as the elastic incoherent structure factor (EISF). If unrestricted translational diffusion involves molecules as a whole, the slower, spatially unconstrained diffusion process can be approximated by Equation (4):

$$T_2(t) = \exp\left[-\frac{t}{\tau_2}\right] \tag{4}$$

where τ_2 is a *q*-dependent relaxation time. The convolution in the energy space is facilitated by the fact that the intermediate scattering functions that we use consist of only time-independent and exponential terms, yielding Equations (5) and (6):

$$F(t) = (1-p)exp\left[-t\left(\frac{1}{\tau_1}+\frac{1}{\tau_2}\right)\right] + p\ exp\left[-\frac{t}{\tau_2}\right] \tag{5}$$

$$S(E) = (1-p)\frac{1}{\pi}\frac{[(\hbar/\tau_1)+(\hbar/\tau_2)]}{E^2+[(\hbar/\tau_1)+(\hbar/\tau_2)]^2} + p\frac{1}{\pi}\frac{(\hbar/\tau_2)}{E^2+(\hbar/\tau_2)^2} \tag{6}$$

The relaxation times for the slow process are thus directly determined from the narrow component, whereas the relaxation times pertinent to the fast process are determined from the difference in the broad and narrow component widths. The parameter *p* is the EISF for the faster, transiently constrained (between the consecutive events associated with the main

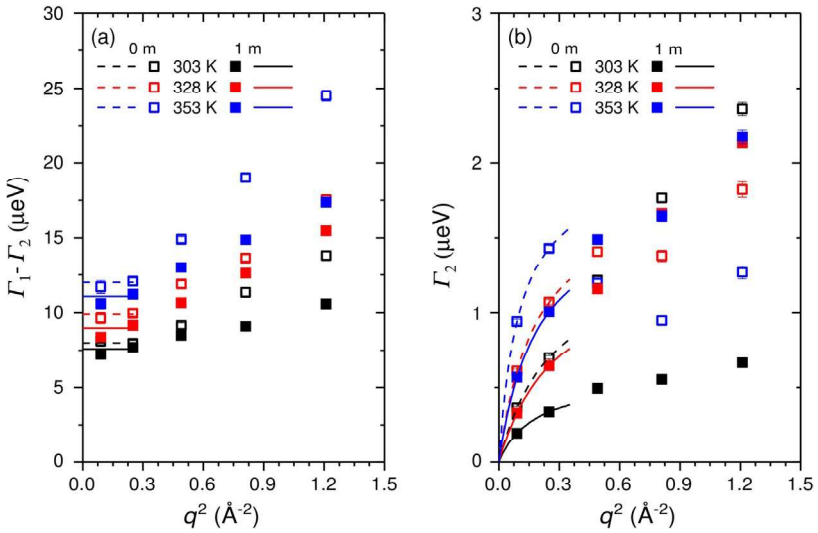

Figure 6. Plots of HWHM for (a) the broad quasi-elastic component ($\Gamma_1-\Gamma_2$) and b) the narrow quasi-elastic component Γ_2 as a function of q^2 for 0 and 1 M salt concentrations at 303, 328, and 353 K. The corresponding lines are fits that were used to calculate the local (a) and translational (b) diffusion coefficients, as described in the text.

structural relaxation), motions of cations. Figure 6 shows the plots of the half-widths at half-maximum (HWHM) as a function of q^2 for 0 and 1 M salt concentrations at different temperatures, as determined from the data fits (performed independently at each q) with Equation (7):

$$I(E) = S(E)*R(E) + (C(E) + D) \qquad (7)$$

where the model dynamic structure factor described by Equation (6) is convolved with the resolution function $R(E)$ and a linear background term is added. The HWHMs are related to the τ parameters in Equation (6) as HWHM $= \hbar/\tau$. The low q behavior of $\Gamma_1-\Gamma_2$ shows a constant HWHM below about 0.4 Å^{-2} (see Figure 6a), which is not observed in the low q behavior of Γ_2 (Figure 6b) and suggests that the faster diffusion process is spatially confined, unlike the slower translational diffusion process. The translational (local or long-range) character of both processes is evident from the increasing HWHM as a function of q^2, as observed in both Figure 6a (local translational motion) and Figure 6b (long-range translational motion).[35]

As is appropriate for localized diffusivity,[36] the faster diffusion coefficients D for $\Gamma=\Gamma_1-\Gamma_2$ were calculated by using the equation $\Gamma = 4.33\,D/a^2$, where a is the confinement radius and $\Gamma_1-\Gamma_2$ was taken as the average of the first two q points, as shown by the horizontal lines in Figure 6a. The confinement radius a was determined from fitting the q-dependent EISF [in this case, the parameter p in Eqs. (5) and (6)] with $c_1 + (1-c_1)\left(\frac{3j_1(qa_1)}{qa_1}\right)^2$ (Figure 7), where j_1 is the spherical Bessel function of the first order and where c_1 describes the "immobile" fraction.[35,37] The confinement radii for the 0 M IL are 3.82, 3.87, and 4.23 Å at 303, 328, and 353 K, respectively. For the 1 M IL these are 3.57, 4.10, and 4.00 Å at 303, 328, and 353 K, respectively. These values were then used to calculate the local diffusion coefficients D associated with the fast component

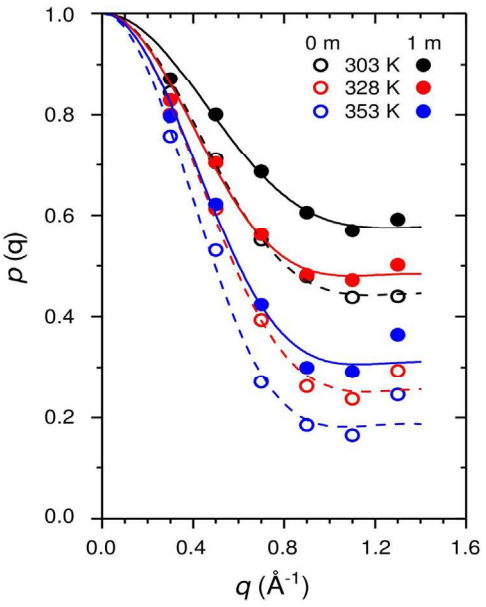

Figure 7. Fits to the EISF $p(q)$ for without and with 1 M Li-TFSI salt concentrations in DMIM-TFSI, at 303 K, 328, and 353 K. The lines, which are fits to the experimental data points (see text), were used to determine the confinement radii for the local diffusion process identified in the QENS data.

from $\Gamma = 4.33\,D/a^2$. Figure 8a shows the temperature dependence of the obtained diffusion coefficients of the faster process (squares), which we assign to a local (confined) process (i.e., motion in the transient cage of the nearest neighbors). These calculated diffusion coefficients, which show slightly smaller values for the 1 M IL, are also listed in Table 1. Similar values have been observed in other IL systems.[10a]

For the slow component, the translational diffusion coefficient D can be determined from the low q data by using the jump diffusion model, HWHM$(q) = (\hbar\tau)(Dq^2/(1+\tau Dq^2)$ (see lines

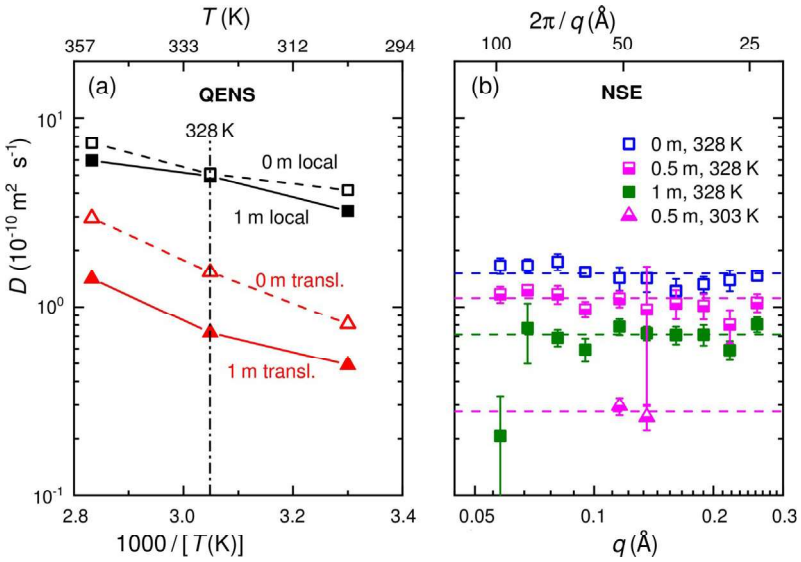

Figure 8. a) Temperature dependence of the diffusion coefficients of the DMIM-TFSI ILs without and with 1 M Li salt, deduced from the QENS measurements (Arrhenius representation). The solid and dashed lines connect the data points. There are two processes, ascribed to local and translational diffusion. b) Momentum-transfer dependence of the diffusion coefficients at 328 K as determined from the NSE experiments. Results are shown for three Li-salt concentrations. For the 0.5 M sample, additional data at 303 K are provided. A single process, proposed to be of translational nature, is observed.

Table 1. Diffusion coefficients calculated from QENS and NSE data.

Li-TFSI concentration [mol L^{-1}]	Temperature [K]	Diffusion coefficient [$\times 10^{-10}$ m^2 s^{-1}]		
		QENS		NSE
		local	translational	average (over q)
0	303	4.16	0.81	–
	328	5.07	1.53	1.51
	353	7.36	2.96	–
0.5	303	–	–	0.28
	328	–	–	1.11
1	303	3.22	0.49	–
	328	4.94	0.73	0.71
	353	5.95	1.41	–

in Figure 6b). The calculated coefficients, plotted in Figure 8a (triangles) and listed in Table 1, again are slightly smaller for the 1 M IL. For both IL samples (0 and 1 M), the local diffusion coefficients are nearly an order of magnitude larger than the translational diffusion coefficients, as may be expected for a shorter-ranged process. The temperature dependence of the local diffusion coefficients in both 0 and 1 M ILs is significantly weaker than that of the translational diffusion coefficients. The local diffusion is relatively independent of the salt concentration, and thus of the bulk viscosity of the IL, as compared with the translational diffusion, which again may be expected considering the length scale of the process.

Comparison can be made with the translational diffusion coefficient of the $DMIM^+$ cation in DMIM-TFSI of about 1×10^{-1} m^{2}s^{-1}at 328 K, deduced from NMR measurements reported in the literature, which is consistent with that calculated from the QENS data.[10a] Triolo et al. similarly reported two distinct processes in the IL BMIM-PF_6, denoted α and β processes; they determined that the faster β process, ascribed to "localized vibrational motions", is essentially temperature independent (250–320 K), whereas our faster process is weakly temperature dependent.[38] We note that caged dynamics, arising from fast motions of the molecules or ions in cages formed by the nearest neighbors, is often termed β relaxation in the literature, like the JG β process discussed above.[12b,39] However, they are not related, and the latter usually arises at much lower frequencies, typically in the hertz-to-megahertz regime.[23]

Generally, NSE spectroscopy should probe the dynamics of the whole DMIM-TFSI system, including cation, anion, and ion aggregates. However, because the neutron scattering cross sections of $TFSI^-$ and Li^+ are much smaller than that of $DMIM^+$, the diffusion coefficients calculated from NSE data are also dominated by the dynamics of $DMIM^+$. The NSE measurements capture slower dynamics at a longer length scale ($q<0.3$ Å^{-1}) than the QENS experiments, and thus only one translational diffusion process is observed. As revealed by Figure 8b, which shows the dependence on momentum transfer for the 0, 0.5, and 1 M ILs, the diffusion coefficients are essentially independent of the length scale measured, but they show significant dependence on temperature and salt concentration. The average diffusion coefficients (average in q) of the 0, 0.5, and 1 M ILs at 328 K are listed in Table 1. We note that the average diffusion coefficients of the 0.5 M IL calculated from the NSE data at 303 K are significantly smaller than those at 328 K, that is, the diffusion is much more strongly influenced by temperature than by salt concentration. The NSE data confirm that the slower diffusion process measured by QENS corresponds to longer-range translational diffusion, with very similar diffusion coefficients determined independently by these different scattering techniques. When the salt concentration increases from 0 to 1 M at 328 K, the diffusion coefficients calculated from the QENS and NSE data decrease by 46 and 53%, respectively. One possible explanation for the slight difference

between the NSE and QENS data in terms of the magnitude of the translational diffusion process is that the QENS data are self-diffusion coefficients of the $DMIM^+$ cations, whereas the additional 7% decrease in the NSE data can be attributed to the ion aggregates.

Comparison of relaxation times, resistivity, and viscosity

Figure 9 shows an Arrhenius representation of the temperature-dependent relaxation times of the IL with 1 M Li-TFSI as deduced in the present work (left scale). The squares show the dielectric α-relaxation time $\tau_{\alpha,\mathrm{diel}}$, determined from the fits shown in Figures 3, 4b and c, and S2. It exhibits clear deviations from simple thermally activated temperature dependence, $\tau \propto \exp[E/(k_B T)]$, in which E is an energy barrier, revealed by its significantly nonlinear behavior in the Arrhenius plot. This is a common phenomenon of glass-forming liquids, often ascribed to an increase in molecular cooperativity with decreasing temperature,[17e,18a,40] and is also often found in ILs.[21a–d,28a] In Figure 9, $\tau_{\alpha,\mathrm{diel}}$ is compared to the dc resistivity ρ_{dc}, also determined from the fits of the dielectric spectra (circles; right scale). The high-temperature part of these data (shown as $\sigma_{dc}=1/\rho_{dc}$) was already presented in Figure 5. Clearly, both data sets can be well scaled onto each other, that is, they are proportional, $\tau_{\alpha,\mathrm{diel}} \propto \rho_{dc}$ (note that the total number of decades is identical for both ordinates in Figure 9, and only the starting value of the ordinate was adapted for the scaling). This finding implies close coupling of the translational ionic motion and the reorientational motion of the dipolar ions in this IL. Such coupling is also found in molecular glass formers with admixed ionic charge carriers[41] and even in ionically conducting plastic crystals.[42]

The $\rho_{dc}(T)$ data cover the broadest and most continuous temperature range of all dynamic quantities deduced in the present work (cf. Figures 9 and 10). Its range is also larger than that of $\tau_{\alpha,\mathrm{diel}}(T)$ because the dc plateau in $\sigma'(\nu)$ can be read off even when the α relaxation has shifted out of the frequency window (Figure 9). However, as discussed above and signified by the temperature-dependent dielectric properties shown in Figure S1, even the 1 M sample seems to exhibit partial crystallization at $T_x \approx 261$ K, albeit much less pronounced than for the other concentrations. Nevertheless, the temperature dependence of ρ_{dc} in Figure 9 at first glance appears smooth and not affected by crystallization. However, a closer look reveals a small change of slope at T_x, indicated by the vertical arrow. Therefore, these data were fitted by two separate VFT laws [Eq. (1) with η replaced by ρ_{dc}] above and below T_x. The fits, shown by the solid and dashed lines in Figure 9, lead to a nearly perfect description of the experimental data.

Figure 10 shows an Arrhenius plot of the high-temperature region of $\rho_{dc}(T)$ for the 1 M IL (full circles; right scale), together with the viscosity data already provided in Figure 2 (full stars;

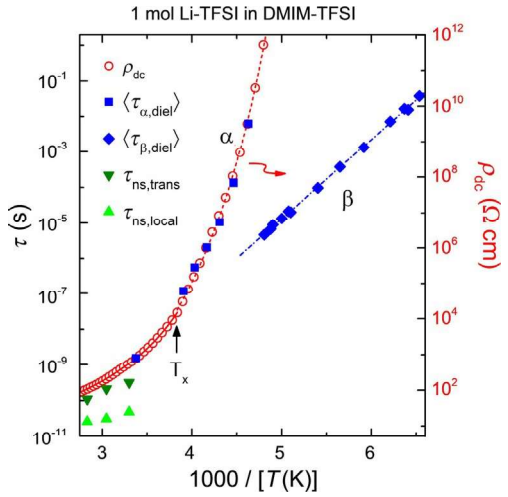

Figure 9. Comparison of the temperature dependences of the relaxation times of DMIM-TFSI mixed with 1 M Li-TFSI (left scale) and of its dc resistivity (circles; right scale), shown in Arrhenius representation. The average α- and β-relaxation times determined from dielectric spectroscopy (squares and diamonds, respectively) and τ, calculated by $\frac{1}{Dq^2}$ with $q=0.8$ Å^{-1}, of the two processes detected by neutron scattering (triangles) are included. The vertical arrow indicates the temperature $T_x=261$ K below which partial crystallization may have occurred (cf. Figure S1). The solid and dashed lines are fits of $\rho(T)$ above and below T_x, respectively, by means of the VFT equation. The dash-dotted line is a linear fit, corresponding to Arrhenius behavior.

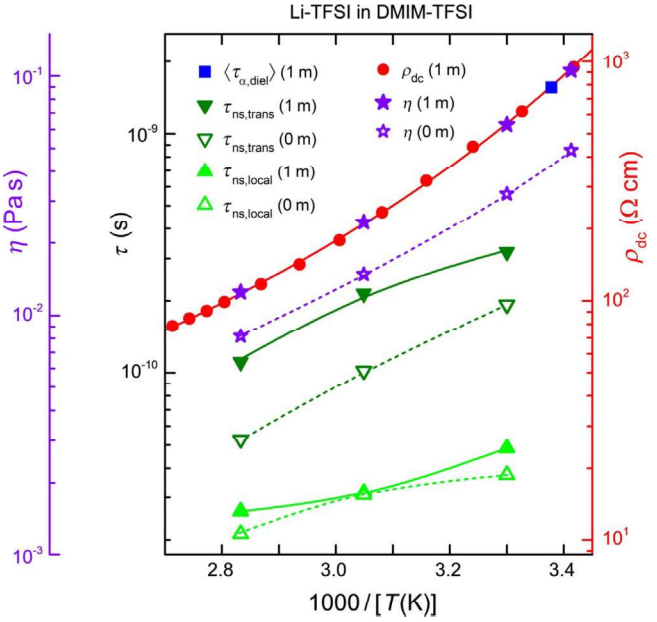

Figure 10. Comparison of the temperature-dependent relaxation times of DMIM-TFSI without and with Li-TFSI (2nd left axis) with the dc resistivity (right axis) and viscosity (1st left axis), all shown in Arrhenius representation. Only the high-temperature range covered by the neutron-scattering experiments is shown (see Figure 9 for ρ_{dc} and $\tau_{\alpha,\mathrm{diel}}$ in an extended temperature range). All three axis ranges were adapted to cover the same number of decades. In addition, the start values of the τ and η ordinates were chosen to achieve an approximate match of $\tau_{\alpha,\mathrm{diel}}(1/T)$ (cf. Figure 9) and $\eta(1/T)$ with the $\rho_{dc}(1/T)$ curve for the 1 M sample. Circles: resistivity for the IL with 1 M Li-TFSI; square: average α-relaxation time of the 1 M sample determined by dielectric spectroscopy; empty and full upright triangles: local relaxation times measured by neutron scattering for 0 and 1 M IL, respectively; empty and full inverted triangles: translational relaxation times for 0 and 1 M IL, respectively; empty and full stars: viscosity for 0 and 1 M Li-TFSI, respectively. The lines are guides to the eye, except that through the ρ_{dc} data points, which represents a VFT fit.

leftmost scale). Clearly, both quantities also can be scaled onto each other, and thus we have $\eta \propto \rho_{dc} \propto \tau_{\alpha,diel}$ for this material. The close coupling of these different dynamic quantities indicates that the temperature dependence of the resistivity (or of the conductivity) is dominated by dynamics, that is, by the temperature dependence of the mobility μ in Equation (2). In contrast, on the basis of these findings, a temperature-dependent variation of the number of free charge carriers n, which could arise from a temperature-dependent variation of the number of cation–anion pairs or aggregates (causing a temperature dependence of the so-called ionicity),[43] seems unlikely.

Clearly, all three ion species can contribute to the resistivity of this IL, albeit most likely with different weight. However, on the basis of dielectric spectroscopy alone, no statement on these contributions can be made. Interestingly, as discussed above, the neutron-scattering results provide access to the translational motion of mainly a single ion species, the $DMIM^+$ cations. The relaxation times of the translational process $\tau_{ns,trans}$ were derived (via $\tau_{ns,trans} \sim \frac{1}{Dq^2}$ with $q = 0.8\ Å^{-1}$) from the corresponding diffusion coefficients determined by QENS for the 1 M ILs (Figure 8a). They are shown by the inverted full triangles in Figures 9 and 10, the latter of which provides an expanded view of the high-temperature region. By taking into account the relation $\eta \propto \rho_{dc} \propto \tau_{\alpha,diel}$ (see discussion above) and using the same relative axis scaling of ρ_{dc} and τ as in Figure 9, the dc-resistivity and viscosity data shown in Figure 10 can be regarded as a reasonable high-temperature extrapolation of the relaxation time $\tau_{\alpha,diel}$, which characterizes the coupled reorientational and translational ionic motion. A comparison with the inverted full triangles in Figure 10 reveals that the translational relaxation measured by QENS is significantly faster than the dynamics measured by the other methods. This decoupling implies that the mobility of the $DMIM^+$ ion, primarily detected by the QENS measurements, is faster than that of the other ions. This is well consistent with the finding of faster cation motion in various ILs, including DMIM-TFSI, based on NMR spectroscopic investigations.[34,10a] Interestingly, such a decoupling seems to be also present for the sample without any Li (cf. empty stars and empty inverted triangles in Figure 10). The smaller overall size of $DMIM^+$ compared with the $TFSI^-$ ion may explain its higher mobility, even in the pure IL. As pointed out in Ref. [10a], the ionic shape also seems to play a role. Of course, the Li^+ ion is far smaller than the two other ions and, naively, a very high mobility may be expected for this ion. However, it can be assumed that its much higher ionic potential increases its interactions with the other ions and therefore considerably reduces its mobility (and that of the other ions; cf. Figure 5 and its discussion).

The local process detected by QENS (upright triangles in Figures 9 and 10) is significantly faster and has clearly a weaker temperature dependence than the coupled resistivity, viscosity, and α relaxation. It thus seems completely unrelated to the ionic charge transport and may be ascribed to local motions within a transient cage formed by the nearest neighbors, as discussed above (cf. Figure 6 and its discussion). Such fast motions play a prominent role in the mode coupling theory of the glass transition[39] and are a well-established experimental finding in spectra of glass-forming liquids, as measured, for example, by neutron scattering.[44] Caged motion is also considered in other theoretical approaches, such as the coupling model.[45]

Finally, the diamonds in Figure 9 indicate the JG β relaxation times $\tau_{\beta,diel} = 1/(2\pi\nu_p)$, determined by reading off the peak positions ν_p in the dielectric loss spectra shown in Figure 3b and (in more detail) in Figure 4a. Perfect Arrhenius behavior is found, which is typical for secondary relaxation processes. A linear fit (dash-dotted line) revealed an energy barrier of $E_\beta \approx 0.44$ eV and a relatively small prefactor $\tau_0 \approx 10^{-16}$ s. In a related imidazolium-based IL with $TFSI^-$ anion, an activation energy of the JG relaxation of similar magnitude was found (0.38 eV).[21e] Interestingly, just as in this material, in our 1 M IL the relation $E_\beta = 24\,k_B T_g$ is well fulfilled for $T_g \approx 208$ K determined from the DSC measurements (Figure 1). This empirical relation was found to be valid in various molecular glass formers.[23a]

Conclusions

By performing neutron-scattering, dielectric, and viscosity measurements we have thoroughly characterized the ionic dynamics in the liquid and supercooled state of a typical imidazolium-based IL with added Li^+ ions. By dielectric spectroscopy, two relaxational processes were detected, which resemble the typical α–β relaxation scenario, well known from molecular glass formers. We ascribe them to the reorientational motions of the dipolar ions and the corresponding JG β relaxation. We found close coupling of the reorientational α relaxation to the viscosity and to the overall translational ionic motion associated with dc charge transport. Clearly, the temperature dependence of the ionic conductivity is dominated by a variation of ion dynamics exhibiting typical glasslike behavior and not by a temperature-dependent ionicity due to the formation of ion aggregates. Even at relatively high Li concentrations, the lithium-salt-doped IL investigated here still shows a high conductivity that is comparable to those of organic liquid electrolytes used in lithium-ion batteries and implies relatively fast ion diffusion.

By QENS, two distinct diffusion coefficients for the $DMIM^+$ ions were detected. The slower process was ascribed to translational diffusion of $DMIM^+$, and the faster process was identified as more local dynamic component, which was confirmed by the NSE data. Comparison with the dielectric, dc, and viscosity results indicates that the translational motion of the $DMIM^+$ ions is faster than the dynamics of the other ions and is increasingly decoupled from the general ionic dynamics at low temperatures. This finding is consistent with earlier NMR investigations[10a,46] and nicely demonstrates that not only the size but also the shape and the ionic potential of an ion determine its mobility. Analysis of the NSE data further suggests that the Li^+ ions move over relatively long distances together with their first coordination shell and that the $DMIM^+$ cations may have a slightly higher net diffusion coefficient than the ion aggregates. The almost constant diffusion rate as a func-

tion of momentum transfer of the 1 M IL as measured by NSE suggests that ion aggregates (the vehicle diffusion mechanism) play an important role in the ion diffusion. The local diffusion process detected by QENS exhibits a weaker dependence on salt concentration, temperature, and bulk viscosity, and clearly plays a minor role in the overall charge transport.

Acknowledgements

This work was supported by the U.S. Department of Energy, Office of Science, Basic Energy Sciences, Materials Sciences and Engineering Division. The neutron scattering experiments at Oak Ridge National Laboratory's (ORNL) Spallation Neutron Source were supported by the Scientific User Facilities Division, Office of Basic Energy Sciences, U.S. Department of Energy (DOE). ORNL is managed by UT-Battelle, LLC, for the U.S. DOE under Contract No. DE-AC05-00OR22725. The work in Augsburg was supported by the Deutsche Forschungsgemeinschaft (Grant No. LU 656/3-1) and by the BMBF via ENREKON. This manuscript has been authored by UT-Battelle, LLC under Contract No. DE-AC05-00OR22725 with the U.S. Department of Energy. The United States Government retains and the publisher, by accepting the article for publication, acknowledges that the United States Government retains a non-exclusive, paid-up, irrevocable, world-wide license to publish or reproduce the published form of this manuscript, or allow others to do so, for United States Government purposes. The Department of Energy will provide public access to these results of federally sponsored research in accordance with the DOE Public Access Plan (http://energy.gov/downloads/doe-public-access-plan).

Conflict of interest

The authors declare no conflict of interest.

Keywords: dielectric spectroscopy · ion dynamics · ionic liquids · lithium · neutron diffraction

[1] a) M. Watanabe, M. L. Thomas, S. G. Zhang, K. Ueno, T. Yasuda, K. Dokko, *Chem. Rev.* **2017**, *117*, 7190–7239; b) N. V. Plechkova, K. R. Seddon, *Chem. Soc. Rev.* **2008**, *37*, 123–150; c) Z. Ma, J. H. Yu, S. Dai, *Adv. Mater.* **2010**, *22*, 261–285; d) S. J. Zhang, J. Sun, X. C. Zhang, J. Y. Xin, Q. Q. Miao, J. J. Wang, *Chem. Soc. Rev.* **2014**, *43*, 7838–7869; e) D. R. MacFarlane, N. Tachikawa, M. Forsyth, J. M. Pringle, P. C. Howlett, G. D. Elliott, J. H. Davis, M. Watanabe, P. Simon, C. A. Angell, *Energy Environ. Sci.* **2014**, *7*, 232–250; f) M. Armand, F. Endres, D. R. MacFarlane, H. Ohno, B. Scrosati, *Nat. Mater.* **2009**, *8*, 621–629; g) Q. W. Yang, Z. Q. Zhang, X. G. Sun, Y. S. Hu, H. B. Xing, S. Dai, *Chem. Soc. Rev.* **2018**, *47*, 2020–2064; h) F. Lo Celso, Y. Yoshida, F. Castiglione, M. Ferro, A. Mele, C. J. Jafta, A. Triolo, O. Russina, *Phys. Chem. Chem. Phys.* **2017**, *19*, 13101–13110; i) O. Russina, F. Lo Celso, N. Plechkova, C. J. Jafta, G. B. Appetecchi, A. Triolo, *Top. Curr. Chem.* **2017**, *375*, 58.

[2] a) A. Lewandowski, A. Swiderska-Mocek, *J. Power Sources* **2009**, *194*, 601–609; b) G. A. Giffin, *J. Mater. Chem. A* **2016**, *4*, 13378–13389; c) X. G. Sun, X. Q. Wang, R. T. Mayes, S. Dai, *ChemSusChem* **2012**, *5*, 2079–2085; d) H. B. Xing, C. Liao, Q. W. Yang, G. M. Veith, B. K. Guo, X. G. Sun, Q. L. Ren, Y. S. Hu, S. Dai, *Angew. Chem. Int. Ed.* **2014**, *53*, 2099–2103; *Angew. Chem.* **2014**, *126*, 2131–2135; e) M. Hog, B. Burgenmeister, K. Bromberger, M. Schuster, S. Riedel, I. Krossing, *ChemElectrochem* **2017**, *4*, 2934–2942; f) X. G. Sun, C. Liao, N. Shao, J. R. Bell, B. K. Guo, H. M. Luo, D. E. Jiang, S. Dai, *J. Power Sources* **2013**, *237*, 5–12; g) D. J. Yoo, J. S. Kim, J. Shin, K. J. Kim, J. W. Choi, *ChemElectrochem* **2017**, *4*, 2345–2351; h) X. G. Sun, Z. Z. Zhang, H. Y. Guan, C. A. Bridges, Y. X. Fang, Y. S. Hu, G. M. Veith, S. Dai, *J. Mater. Chem. A* **2017**, *5*, 6589–6596; i) X. G. Sun, Z. H. Bi, H. S. Liu, Y. X. Fang, C. A. Bridges, M. P. Paranthaman, S. Dai, G. M. Brown, *Chem. Commun.* **2016**, *52*, 1713–1716; j) C. A. Bridges, X. G. Sun, B. K. Guo, W. T. Heller, L. L. He, M. P. Paranthaman, S. Dai, *ACS Energy Lett.* **2017**, *2*, 1698–1704.

[3] a) C. Liao, N. Shao, K. S. Han, X. G. Sun, D. E. Jiang, E. W. Hagaman, S. Dai, *Phys. Chem. Chem. Phys.* **2011**, *13*, 21503–21510; b) K. Hayamizu, Y. Aihara, H. Nakagawa, T. Nukuda, W. S. Price, *J. Phys. Chem. B* **2004**, *108*, 19527–19532.

[4] a) T. Frömling, M. Kunze, M. Schönhoff, J. Sundermeyer, B. Roling, *J. Phys. Chem. B* **2008**, *112*, 12985–12990; b) F. F. Chen, M. Forsyth, *Phys. Chem. Chem. Phys.* **2016**, *18*, 19336–19344; c) M. Forsyth, G. M. A. Girard, A. Basile, M. Hilder, D. R. MacFarlane, F. Chen, P. C. Howlett, *Electrochim. Acta* **2016**, *220*, 609–617.

[5] a) Z. Li, G. D. Smith, D. Bedrov, *J. Phys. Chem. B* **2012**, *116*, 12801–12809; b) O. Borodin, G. D. Smith, W. Henderson, *J. Phys. Chem. B* **2006**, *110*, 16879–16886; c) J. B. Haskins, C. W. Bauschlicher, J. W. Lawson, *J. Phys. Chem. B* **2015**, *119*, 14705–14719.

[6] a) J. Pitawala, A. Martinelli, P. Johansson, P. Jacobsson, A. Matic, *J. Non-Cryst. Solids* **2015**, *407*, 318–323; b) L. J. Hardwick, M. Holzapfel, A. Wokaun, P. Novak, *J. Raman Spectrosc.* **2007**, *38*, 110–112; c) J. C. Lassegues, J. Grondin, C. Aupetit, P. Johansson, *J. Phys. Chem. A* **2009**, *113*, 305–314.

[7] a) F. Castiglione, E. Ragg, A. Mele, G. B. Appetecchi, M. Montanino, S. Passerini, *J. Phys. Chem. Lett.* **2011**, *2*, 153–157; b) K. Hayamizu, S. Tsuzuki, S. Seki, *J. Chem. Eng. Data* **2014**, *59*, 1944–1954.

[8] M. Gouverneur, J. Kopp, L. van Wullen, M. Schonhoff, *Phys. Chem. Chem. Phys.* **2015**, *17*, 30680–30686.

[9] M. L. P. Le, F. Alloin, P. Strobel, J. C. Lepretre, C. P. del Valle, P. Judeinstein, *J. Phys. Chem. B* **2010**, *114*, 894–903.

[10] a) H. Tokuda, K. Hayamizu, K. Ishii, M. Susan, M. Watanabe, *J. Phys. Chem. B* **2005**, *109*, 6103–6110; b) C. W. Do, X. G. Sun, C. J. Jafta, S. Dai, M. Ohl, E. Mamontov, *Sci. Rep.* **2018**, *8*, 10354.

[11] P. Sippel, V. Dietrich, D. Reuter, M. Aumüller, P. Lunkenheimer, A. Loidl, S. Krohns, *J. Mol. Liq.* **2016**, *223*, 635.

[12] a) R. Böhmer, M. Maglione, P. Lunkenheimer, A. Loidl, *J. Appl. Phys.* **1989**, *65*, 901–904; b) P. Lunkenheimer, U. Schneider, R. Brand, A. Loid, *Contemp. Phys.* **2000**, *41*, 15–36.

[13] M. Ohl, M. Monkenbusch, N. Arend, T. Kozielewski, G. Vehres, C. Tiemann, M. Butzek, H. Soltner, U. Giesen, R. Achten, H. Stelzer, B. Lindenau, A. Budwig, H. Kleines, M. Drochner, P. Kaemmerling, M. Wagener, R. Möller, E. B. Iverson, M. Sharp, D. Richter, *Nucl. Instrum. Methods Phys. Res., Sect. A* **2012**, *696*, 85–99.

[14] E. Mamontov, K. W. Herwig, *Rev. Sci. Instrum.* **2011**, *82*, 085109.

[15] a) W. Xu, L. M. Wang, R. A. Nieman, C. A. Angell, *J. Phys. Chem. B* **2003**, *107*, 11749–11756; b) C. A. Angell, Y. Ansari, Z. F. Zhao, *Faraday Discuss.* **2012**, *154*, 9–27.

[16] H. Matsumoto, H. Sakaebe, K. Tatsumi, M. Kikuta, E. Ishiko, M. Kono, *J. Power Sources* **2006**, *160*, 1308–1313.

[17] a) H. Vogel, *Phys. Z.* **1921**, *22*, 645; b) G. S. Fulcher, *J. Am. Ceram. Soc.* **1923**, *8*, 339–355; c) G. Tammann, W. Hesse, *Z. Anorg. Allg. Chem.* **1926**, *156*, 245–257; d) Fast Ion Conductors in Viscous Liquids and Glasses: C. A. Angell in *Relaxations in Complex Systems* (Eds.: K. Ngai, G. B. Wright), National Technical Information Service, U.S. Department of Commerce, Springfield, VA 22161, **1985**, p. 3; e) M. D. Ediger, C. A. Angell, S. R. Nagel, *J. Phys. Chem.* **1996**, *100*, 13200–13212.

[18] a) G. Adam, J. H. Gibbs, *J. Chem. Phys.* **1965**, *43*, 139–146; b) M. Galiński, A. Lewandowski, I. Stępniak, *Electrochim. Acta* **2006**, *51*, 5567–5580.

[19] S. Emmert, M. Wolf, R. Gulich, S. Krohns, S. Kastner, P. Lunkenheimer, A. Loidl, *Eur. Phys. J. B* **2011**, *83*, 157.

[20] a) P. Lunkenheimer, A. Loidl, *Chem. Phys.* **2002**, *284*, 205–219; b) A. Schönhals, F. Kremer in *Broadband Dielectric Spectroscopy* (Eds.: F. Kremer, A. Schönhals), Springer, Berlin, Heidelberg, **2003**, pp. 35–57.

[21] a) P. Sippel, P. Lunkenheimer, S. Krohns, E. Thoms, A. Loidl, *Sci. Rep.* **2015**, *5*, 13922; b) E. Thoms, P. Sippel, D. Reuter, M. Weiß, A. Loidl, S. Krohns, *Sci. Rep.* **2017**, *7*, 7463; c) C. Krause, J. Sangoro, C. Iacob, F. Kremer, *J. Phys. Chem. B* **2009**, *114*, 382–386; d) A. Rivera, A. Brodin, A. Pugachev, E. Rössler, *J. Chem. Phys.* **2007**, *126*, 114503; e) A. Rivera, E. A.

Rössler, *Phys. Rev. B* **2006**, *73*, 212201; f) J. Hunger, A. Stoppa, S. Schrödle, G. Hefter, R. Buchner, *ChemPhysChem* **2009**, *10*, 723 – 733; g) C. Gainaru, E. W. Stacy, V. Bocharova, M. Gobet, A. P. Holt, T. Saito, S. Greenbaum, A. P. Sokolov, *J. Phys. Chem. B* **2016**, *120*, 11074 – 11083.
[22] P. J. Griffin, A. L. Agapov, A. P. Sokolov, *Phys. Rev. E* **2012**, *86*, 021508.
[23] a) A. Kudlik, S. Benkhof, T. Blochowicz, C. Tschirwitz, E. Rössler, *J. Mol. Struct.* **1999**, *479*, 201 – 218; b) S. Kastner, M. Köhler, Y. Goncharov, P. Lunkenheimer, A. Loidl, *J. Non-Cryst. Solids* **2011**, *357*, 510 – 514.
[24] G. P. Johari, M. Goldstein, *J. Chem. Phys.* **1970**, *53*, 2372 – 2388.
[25] a) F. H. Stillinger, *Science* **1995**, *267*, 1935 – 1939; b) J. S. Harmon, M. D. Demetriou, W. L. Johnson, K. Samwer, *Phys. Rev. Lett.* **2007**, *99*, 135502.
[26] D. W. Davidson, R. H. Cole, *J. Chem. Phys.* **1951**, *19*, 1484 – 1490.
[27] P. Macedo, *Phys. Chem. Glasses* **1972**, *13*, 171 – 179.
[28] a) N. Ito, W. Huang, R. Richert, *J. Phys. Chem. B* **2006**, *110*, 4371 – 4377; b) G. Jarosz, M. Mierzwa, J. Zioło, M. Paluch, H. Shirota, K. Ngai, *J. Phys. Chem. B* **2011**, *115*, 12709 – 12716.
[29] a) S. Elliott, *J. Non-Cryst. Solids* **1994**, *170*, 97 – 100; b) B. Roling, *J. Non-Cryst. Solids* **1999**, *244*, 34 – 43; c) I. Hodge, K. Ngai, C. Moynihan, *J. Non-Cryst. Solids* **2005**, *351*, 104 – 115.
[30] S. Seki, Y. Ohno, Y. Kobayashi, H. Miyashiro, A. Usami, Y. Mita, H. Tokuda, M. Watanabe, K. Hayamizu, S. Tsuzuki, M. Hattori, N. Terada, *J. Electrochem. Soc.* **2007**, *154*, A173 – A177.
[31] C. A. Angell, *Electrochim. Acta* **2017**, *250*, 368 – 375.
[32] Z. Wojnarowska, Y. Wang, K. J. Paluch, A. P. Sokolov, M. Paluch, *Phys. Chem. Chem. Phys.* **2014**, *16*, 9123 – 9127.
[33] X. G. Sun, S. Wan, H. Y. Guang, Y. X. Fang, K. S. Reeves, M. F. Chi, S. Dai, *J. Mater. Chem. A* **2017**, *5*, 1233 – 1241.
[34] *Neutron Applications in Earth, Energy and Environmental Sciences* (Eds.: L. Liang, R. Rinaldi, H. Schober), Springer, Boston, MA, **2009**.
[35] E. Mamontov, H. Luo, S. Dai, *J. Phys. Chem. B* **2009**, *113*, 159 – 169.
[36] M. C. Bellissent-Funel, S. H. Chen, J. M. Zanotti, *Phys. Rev. E* **1995**, *51*, 4558 – 4569.
[37] E. Mamontov, G. A. Baker, H. Luo, S. Dai, *ChemPhysChem* **2011**, *12*, 944 – 950.
[38] A. Triolo, O. Russina, V. Arrighi, F. Juranyi, S. Janssen, C. M. Gordon, *J. Chem. Phys.* **2003**, *119*, 8549 – 8557.
[39] W. Gotze, L. Sjogren, *Rep. Prog. Phys.* **1992**, *55*, 241.
[40] a) P. G. Debenedetti, F. H. Stillinger, *Nature* **2001**, *410*, 259; b) T. Kirkpatrick, P. Wolynes, *Phys. Rev. B* **1987**, *36*, 8552; c) T. Bauer, P. Lunkenheimer, A. Loidl, *Phys. Rev. lett.* **2013**, *111*, 225702.
[41] M. Köhler, P. Lunkenheimer, A. Loidl, *Eur. Phys. J. E* **2008**, *27*, 115.
[42] a) K. Geirhos, P. Lunkenheimer, M. Michl, D. Reuter, A. Loidl, *J. Chem. Phys.* **2015**, *143*, 081101; b) D. Reuter, C. Geiß, P. Lunkenheimer, A. Loidl, *J. Chem. Phys.* **2017**, *147*, 104502.
[43] D. R. MacFarlane, M. Forsyth, E. I. Izgorodina, A. P. Abbott, G. Annat, K. Fraser, *Phys. Chem. Chem. Phys.* **2009**, *11*, 4962 – 4967.
[44] a) W. Knaak, F. Mezei, B. Farago, *EPL (Europhysics Letters)* **1988**, *7*, 529; b) J. Wuttke, J. Hernandez, G. Li, G. Coddens, H. Cummins, F. Fujara, W. Petry, H. Sillescu, *Phys. Rev. Lett.* **1994**, *72*, 3052.
[45] K. Ngai, *J. Phys. Condens. Matter* **2003**, *15*, S1107.
[46] H. Every, A. Bishop, M. Forsyth, D. MacFarlane, *Electrochim. Acta* **2000**, *45*, 1279 – 1284.